MDPI

Article

Utilization of Mechanical Resonance for the Enhancement of Slider-Crank Mechanism Dynamics in Gas Compression Processes

Wiesław Fiebig * and Willy Prastiyo

Faculty of Mechanical Engineering, Wrocław University of Science and Technology, Łukasiewicza 5/7, 50-370 Wrocław, Poland
* Correspondence: wieslaw.fiebig@pwr.edu.pl; Tel.: +48-71-3202700

Abstract: In the slider-crank mechanism, where the rotational motion is transformed into the translational motion, the input torque is highly variable due to the inertial effect. The consequence of fluctuating torque is that it causes the load upon the prime mover to be inconsistent, which might likely results in higher stresses in the components, higher joint friction, and the necessity for higher driving power. In this paper, a technique of reduction of the dynamic torque and joint forces in the slider-crank mechanism using mechanical resonance is described. A comparative result of the conventional system in the process of gas compression, as a practical application example, is presented. The result shows that the utilization of resonance has the advantage of providing lower dynamic torque and rotating joint forces compared to the conventional operation. Since the compression of the air itself takes effect as a spring compression, in the gas compression process, the narrow torque and force region around the resonant frequency can be obtained with or without the use of spring as the element for storing the potential energy.

1. Introduction

1.1. Background

The contemporary and has not ended scientific concern in the present day is the enhancement of energy efficiency [1]. After energy saving, energy efficiency is the second top priority of the sustainable energy hierarchy. As machines are the major device that uses energy to perform the intended function, regardless of their application, improving their efficiency is of utmost importance. In manufacturing, for example, excellent efficiency of working machines can result in reducing costs and improving throughput [2,3]. A case study performed at a Swedish paper mill showed that a paper mill machine could generate an extra profit of at least 7.8 million Swedish kronor (approximately US$ 0.975 million) per year, or around 12.5% of its yearly maintenance budget, provided that the machine runs at a favorable extent of efficiency [3].

The effectiveness of a machine in transforming the power input to the device into power output holds a crucial role in the achievement of maximum efficiency. Enhancements in the energy efficiency of the machines could conceivably be achieved by embracing a more efficient technology to reduce energy losses [4,5]. Moreover, periodic maintenance could then help the machine prolong its life and maintain its working efficiency [6]. While the slider-crank mechanism is the most widely applied machine element [7] for converting rotational motion into reciprocating motion, or vice versa, enhancing its working efficiency could be a notable benefit in the improvement of energy conservation.

1.2. Problem of Interest

When a slider-crank mechanism operates, in which the rotation of its crank drives the linear movement of the slider, the dynamic (reaction) torque arises when the slider

translationally accelerates or decelerates [8,9]. Positive and negative values of torque at a certain crank angle are involved in accelerating the slider from the bottom dead center (BDC) to approximately the middle of the stroke, as well as when decelerating from the middle to the top dead center (TDC), and so on throughout the cycle [10,11]. In the idealized condition where the dissipative forces are inexistent, the net value of the power consumption within one crank revolution is obviously zero; the energy transfer is conserved over time. However, in physical actuality, higher dynamic torque due to the inertial forces can result in higher energy dissipation that arises from joint friction and component internal stresses. In the end, higher energy dissipation will lead to a lower system's energy efficiency.

The resonance phenomenon is commonly utilized in a beneficial way in order to efficiently administer the supplied energy in the discipline of electricity and optics [12–14], but it is commonly understood as an undesirable phenomenon in the field of mechanics [15–17] and in civil engineering (i.e., Tacoma Bridge). Mechanical resonance may cause violent vibrations in improperly constructed structures, which may end in component failure or other related catastrophic consequences.

Even so, in this article, an approach specifically for the slider-crank mechanism is presented in which the phenomenon of resonance can actually be employed to reduce the dynamic torque to improve the system's efficiency.

1.3. Literature Review

Resonance is mostly known as an unwanted phenomenon in a mechanical system. For example, modal tests conducted by Sinha and Rao [18] on the complete assembly of pumps and piping layout identified that resonance is the root cause of the failure of mechanical coupling between the motor and pump rotors. In a piezoelectric accelerometer, Ghemari et al. [19] confirm that the resonance phenomenon effect must be minimized to prevent failure. To solve the resonance problem, El-Gazzar [20] recommends increasing the structural stiffness of a vertical pump yet may, in turn, increase the weight or the need for better material quality.

Nevertheless, despite the common concern that the resonance phenomenon in most mechanical structures is unwanted, a minor amount of studies show that the resonance in a mechanical system can, in fact, be utilized to obtain a beneficial outcome. Franca and Weber [21] have studied the use of mechanical resonance in a drilling technique called resonance hammer drilling. In their study, the resonance phenomenon was utilized to increase the rate of penetration (ROP) in hard rock drilling. Despotovic et al. [22] show that the resonant mode of the vibratory conveyor with electromagnetic excitation consumed less energy when maintaining the system in the state of resonance. Aiple, M., et al. [23] show that if the excitation frequency and resonance frequency are equal with a flexible (Series Elastic Actuator-based) hammer, teleoperators can reach peak velocities of more than 200% higher than peak velocities with a rigid hammer. In comparison to a rigid hammer driven by the same velocity source, a flexible hammer's peak velocity and peak energy are substantially higher when the mechanical resonance of the hammer is excited. Fiebig and Wróbel [24], based on their simulation and experiment, found that the impact machine, which uses mechanical resonance with a resonant block and spring element, has a significant reduction of energy demand in comparison with the conventional machine, which uses a slider-crank and flywheel coupling. In [25], the modeling of the resonant linear compressor has been presented, and it stated that the efficiency of such a compressor could achieve higher values.

Some work has been performed proposing the balancing methods of the slider-crank mechanism. Arakelian, V. [10] uses the ideal connection of two identical slider-crank systems to address the issue of input torque fluctuation. This is accomplished by reducing the coupled linkages' input torque root-mean-square value. He demonstrated that the values of the coupling angles of the two mechanisms around 90 degrees offer the greatest results in terms of minimizing input torque. Another study by Arakelian and Briot [26]

puts out a design idea that enables slider-crank devices to simultaneously balance shaking force/shaking moment and torque. Initially, the cam mechanism carrying a counterweight cancels the shaking force and shaking moment. Then, torque is minimized by using the spring provided for keeping contact in this balancing cam mechanism.

1.4. Scope and Contribution of the Study

Essentially, during resonance, the driven elements in the mechanical system tend to effectively receive the provided kinetic energy when the frequency of its repetitive movement about a central value matches the system's natural frequency. In this sense, if proper techniques for the exploitation of mechanical resonance are applied in the system, the dynamic torque acting upon the prime mover, which includes the crankshaft and motor, could be optimally reduced regardless of the inertial forces of the slider as the driven element throughout the condition of resonance.

A barrier that inhibits the use of resonance in machine operation is inadequate information on what manner the resonance phenomenon can be advantageous for the slider-crank mechanism, not solely in the way of how the resonance should be prevented to maintain structural integrity. While mechanical resonance has been the subject of numerous studies on structural integrity and failure, the information presented within this article is expected to be a novel concept, answering the question of how the slider-crank mechanism can be dynamically more efficient.

In this article, the approach will be made through modification of the conventional slider-crank design. Particularly, the reciprocating compressor (or piston compressor) is discussed as the practical study example since it represents the common application of a slider-crank mechanism that has varying external loads. Method of numerical simulation, which includes multibody dynamics simulation and multi-domain systems simulation, is employed to model, analyze, and estimate the performance of the designed system. Moreover, a physical prototype is built for verification. To summarize, the contributions of this study are as follows: (a) method of the utilization of mechanical resonance in the slider-crank mechanism is described, especially in the case of power transmission from the crank to the slider; (b) comparative results of the system with and without the use of mechanical resonance are presented.

1.5. Organization of the Article

The rest of this article is organized as follows: Section 2, which mainly describes the method of conducting the study, consists of Section 2.1, the scheme of simulation and experimental verification; Section 2.2, modeling and simulation configuration, including the description of the underlying equations that govern the simulation; Section 2.3, description of the built physical prototype. Moreover, Section 3, which also comprises several subsections, shows the results of the analysis based on the multi-domain system simulation (Section 3.1), multibody dynamics simulation (Section 3.2), and tests of the physical prototype (Section 3.3). Finally, the conclusion of this study is presented in Section 4.

2. Methods

2.1. Scheme

Initially, a reciprocating compressor CAD model is prepared and imported into MSC ADAMS/View. As shown in Figure 1, the model consists of the crankshaft as the crank and the crosshead, push rod, and piston as the slider. Connecting rod is the component that connects the crank to the slider. Coil springs envelop the rails, fixed to the main frame and the crosshead so that, at the equilibrium position, the slider is at the middle of the stroke. The mass and moment of inertia of each part of the model are set to the determined properties. Joints, including their friction properties, are made to connect each contributing part, which turns the CAD into a multibody dynamics (MBD) model. Moreover, since ADAMS cannot simulate the dynamics of the fluid, an equivalent multi-domain system

sketch of the CAD model is also built in Simcenter Amesim to obtain the air suction and compression forces upon the piston.
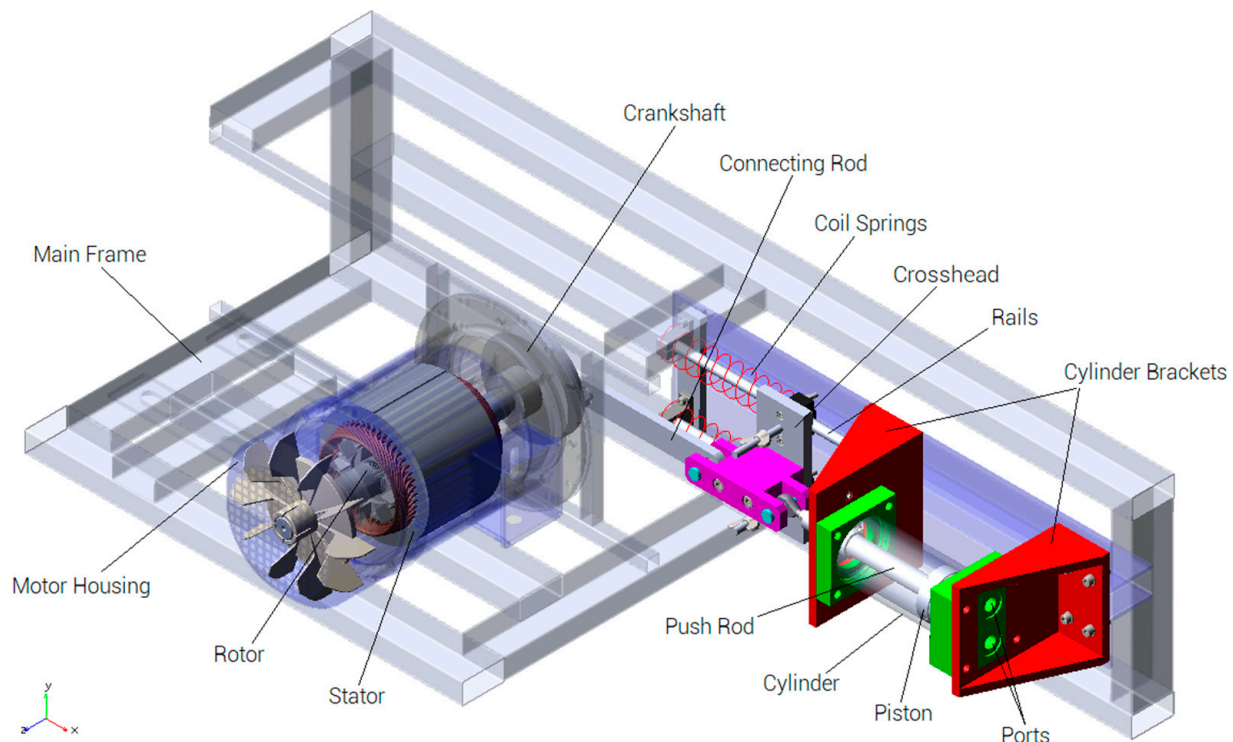

Figure 1. CAD-MBD model of the reciprocating compressor prototype. Electric motor is adapted from [27].

At first, the data of crank angular position versus the force at the top of the piston caused by the air suction and compression processes are exported from the Amesim simulation results to ADAMS. In ADAMS, the imported simulation data from Amesim are received as a spline, which will be employed as the working single-component applied force at the top of the piston of the MBD model. Multibody simulations are performed in two main operation setups: (1) without spring and (2) with spring; both have comparable component specifications and constraints. In the form of the full assembly, MBD models are calculated by the effort estimation tools to assess the dynamic torque and power consumption. Furthermore, the influences of the following different minor operation setups on the system's performance are analyzed: frictional force, pressure loads, component masses, and operating speeds. After all, comparative results of the system's efficiency with and without the use of mechanical resonance are presented. Based on the findings of the computer simulations, a physical prototype is built for validation. Finally, both computer simulations and physical prototype experimental results are evaluated for further possible studies and development.

2.2. Modeling and Simulation Configuration

2.2.1. Multi-Domain System Model

Multi-domain system modeling and simulations are performed to obtain the air pressure and hence, forces upon the piston due to suction and compression strokes. As depicted in Figure 2, the model consists of 16 components of the sketch, which have parameters shown in Table 1. Prime mover (1) rotates the crank of component 4, which is then converted into translational motion to move the piston (5). When the piston moves from TDC to BDC, the pressure differential causes the inlet valve (9, the one below) to open; the air is sucked into the cylinder. The air inside the cylinder is then pumped out through the outlet valve (9, above) into the tank (14). A relief valve (13) is used to limit the upstream

pressure within the pneumatic circuit and thus protect the pneumatic components from overpressure. Each simulation step size and duration in the multi-domain system should be synchronized with the multibody dynamics simulation. The thermal exchange coefficient is set to 0 J/m²/K/s as heat exchange is not considered the major concern in this study. Component 4 is a perfect converter between rotary and linear motion with no frictional loss or inertia. In component 5, the rod diameter d_r is set to zero since there is no rod at the top of the piston. Current chamber length s (Equation (1)) and volume of the chamber V (Equation (2)) are calculated as

$$s = x_0 - x \tag{1}$$

$$V = \frac{s\pi}{4}\left(d_p{}^2 - d_r{}^2\right) \tag{2}$$

while the total force acting toward the connecting rod F_l is calculated by (Equation (3))

$$F_l = \frac{p_l \pi}{4}\left(d_p{}^2 - d_r{}^2\right) \tag{3}$$
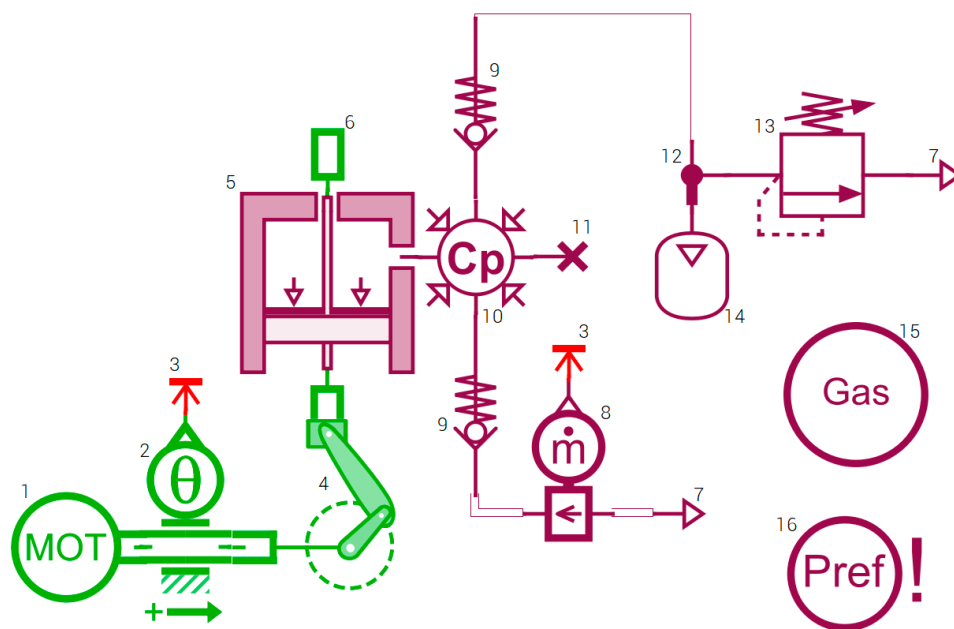
Figure 2. Multi-domain system sketch of the reciprocating compressor prototype.

Table 1. Parameters for the simulations of the presented multi-domain system sketch.

	Components	Parameters	Value
1	Constant-speed prime mover	Shaft speed	[a] -
2	Angular displacement sensor	Sign convention: positive from	Port 1 to 3
		Offset to be subtracted from angle	0 degree
		Gain for signal output	1/degree
3		Plug for signal port	
4	Ideal crank without friction or inertia with state variable	Angular position of crank (initial)	0 degree
		Radius of crank	50 mm
		Length of connecting rod	168 mm
		Offset of displacement	0 mm
		Offset perpendicular to displacement	0 mm

	Components	Parameters	Value
5	Pneumatic piston	Piston diameter	60 mm
		Rod diameter	0 mm
		Chamber length at zero displacement	0 mm
6	Zero force source		
7	Source of atmospheric pressure and temperature	Temperature at port 1	293.15 K
8	Pneumatic mass flow sensor	Offset to be subtracted from mass flow	0 g/s
		Gain for signal output	1/(g/s)
9	Pneumatic check valve with saturation (suction valve)	Maximum flow coefficient (Cv)	22 (inlet), 20 (outlet)
		Check valve cracking pressure	0 bar (both inlet and outlet)
		Maximum opening pressure	1 bar (both inlet and outlet)
		Valve hysteresis	0 bar (both inlet and outlet)
10	Variable volume pneumatic chamber with heat exchange	Dead volume	0.62 L
		Thermal exchange coefficient	0 J/m^2/K/s
		Thermal exchange area	0.1 m^2
11	Zero pneumatic flow source		
12	Pneumatic junction three ports		
13	Pneumatic relief valve	Relief valve cracking pressure	[a] -
		Relief valve mass flow rate pressure gradient	10 g/s/bar
		Valve hysteresis	0 bar
14	Fixed volume pneumatic chamber with heat exchange	Volume	1 L
		Thermal exchange coefficient	0 J/m^2/K/s
		Thermal exchange area	0.1 m^2
15	Generic gas definition	Specific heat ratio	1.4
		Specific gas constant	287 J/kg/K
		Absolute viscosity	0.0182 cP
		Thermal conductivity	0.0264 W/m/K
		Enthalpy of formation	−125.53 J/mol
		Properties definition	Air, perfect gas
16	Set reference pressure	Reference pressure	1.013 barA

[a] depends on the setup and comparison scenario.

The pneumatic check valve (9) is normally closed. It opens and lets the air flow through the valve when the pressure drop across the valve exceeds the cracking pressure. The maximum opening pressure is the pressure differential at which the valve is fully open, which is greater than the cracking pressure. In the simulation, for computation efficiency, the pneumatic valve dynamics parameter is set to static behavior, i.e., no dynamic is modeled. The valve net opening pressure Δp is given by Equation (4)

$$\Delta p = p_2 - p_1 - p_c. \tag{4}$$

The static fractional valve opening of the valve o_v is given by Equation (5)

$$o_v = \frac{\Delta p}{p_{max} - p_c} \tag{5}$$

The relief valve (13) works rather comparably to the check valve, with the aim that the pressure drop gets regulated to the cracking pressure. The opening of the relief valve is determined by the pressure drop p_d (Equation (6))

$$p_d = p_2 - p_1 - p_c. \tag{6}$$

If $p_d \leq 0$, the relief valve is closed, and the flow rates are null. Otherwise, the relief valve is open. The relief valve mass flow rate pressure gradient G is defined as (Equation (7))

$$G = \frac{\dot{m}_d}{p_d} \tag{7}$$

To define the gas characteristics in the pneumatic circuit, component 15 is used. The property of the perfect gas is used in the simulation of this study. The equation of state is pointed out in Equation (8)

$$p = \frac{R \cdot T}{V} \tag{8}$$

2.2.2. Multibody Dynamics Model

Specification of each part of the model is set to the appropriate properties, as shown in Table 2. Except for the piston, push rod, crosshead, connecting rod, and crankshaft, the component's mass and moment of inertia are defined by ADAMS/View based on their geometry and material type. ADAMS/View numerically composes and resolves the system equations as functions of time based on the principles of Lagrangian dynamics using Lagrange's equations of the second form (Euler–Lagrange equations) [28]. The Lagrangian function for a system is the difference in the total kinetic energy and the total potential energy of the system. The Euler–Lagrange equation is given as (Equation (9))

$$\frac{d}{dt}\left(\frac{\partial \mathcal{L}}{\partial \dot{q}_j}\right) = \frac{\partial \mathcal{L}}{\partial q_j} \tag{9}$$

By referring to Figure 3, the general solution of this reciprocating compressor prototype consists of point masses of the crankshaft (m_1); connecting rod (m_2); crosshead (m_3); and pushrod, piston, and piston pin unit (m_4). The total kinetic energy of the system, T, is the sum of the rotational kinetic energy of m_1 along α (rotating around center A); the translational kinetic energy of m_2 along x_2; rotational kinetic energy of m_2 along β (rotating around joint C); the translational kinetic energy of m_3 along x_3; and translational kinetic energy of m_4 along x_4. In this assembly, the magnitude of $x_2 = x_3 = x_4 = x$, and $m_2 + m_3 + m_4 = M$, so that T is defined as (Equations (10) and (11))

$$T = \frac{1}{2}I_1\dot{\alpha}^2 + \frac{1}{2}m_2\dot{x}_2^2 + \frac{1}{2}I_2\dot{\beta}^2 + \frac{1}{2}m_3\dot{x}_3^2 + \frac{1}{2}m_4\dot{x}_4^2 \tag{10}$$

$$T = \frac{1}{2}I_1\dot{\alpha}^2 + \frac{1}{2}I_2\dot{\beta}^2 + \frac{1}{2}\dot{x}^2 M \tag{11}$$

The motion of the piston, crosshead, and connecting rod is obtained in relation to the crankshaft rotation so that the translational displacement x, angular displacement β, and velocity $\dot{\beta}$ are (Equations (12), (13), and (14), respectively)

$$x = l_1 - l_1 \cos \alpha + l_2 - l_2 \cos \beta \tag{12}$$

$$\beta = \arcsin\left(\frac{l_1}{l_2}\sin \alpha\right) \tag{13}$$

$$\dot{\beta} = \frac{\dot{\alpha} l_1 \cos \alpha}{\sqrt{l_2^2 - l_1^2 \sin^2 \alpha}} \tag{14}$$

Table 2. Components' dimensions, mass, and moment of inertia.

Essential Dimensions					
Part	**Link**	**Length (mm)**			
Crank radius l_1	AB	50			
Connecting rod length l_2	BC	168			

| Mass and moment of inertia					
Part	**Mass (kg)**	**Moment of Inertia (kg.mm^2)**		**Connected with**	**Joint**
		I_{xx}	**I_{yy}**	**I_{zz}**	
Main frame	24.59	3.08×10^6	2.80×10^6	5.76×10^5	Ground	Fixed
Stator	2.80	1.103×10^4	8562.18	8555.26	Motor housing	Fixed
Connecting rod	0.15 [b]	451.95	441.64	12.76	Crankshaft	Revolute
					Crosshead	Revolute
Crankshaft	0.85 [b]	1350.89	798.75	772.66	Connecting rod	Revolute
					Rotor	Fixed
Cylinder	1.53	4056.40	4054.44	1688.46	Cylinder brackets	Fixed
					Piston	Cylindrical
Front cylinder bracket	4.13	1.59×10^4	1.07×10^4	7412.01	Main frame	Fixed
					Cylinder	Fixed
Motor housing	2.12	1.69×10^4	1.62×10^4	1.37×10^4	Main frame	Fixed
					Rotor	Fixed
Piston (including pin)	0.25 [b]	335.87	292.34	290.84	Push rod	Fixed
					Cylinder	Cylindrical
Push rod	0.25 [b]	2358.69	2357.44	35.95	Piston	Fixed
					Crosshead	Revolute
Rail	1.22	1.89×10^4	1.66×10^4	2664.15	Main frame	Revolute
					Crosshead	Translational
Rear cylinder bracket	3.93	1.90×10^4	1.09×10^4	1.01×10^4	Main frame	Fixed
					Cylinder	Fixed
Rotor	2.59	1.32×10^4	1.32×10^4	2554.61	Crankshaft	Fixed
					Motor housing	Revolute
Crosshead	varied	4850.21	4338.28	3509.18	Rail	Translational
					Connecting rod	Revolute
					Push rod	Revolute

[b] user defined.
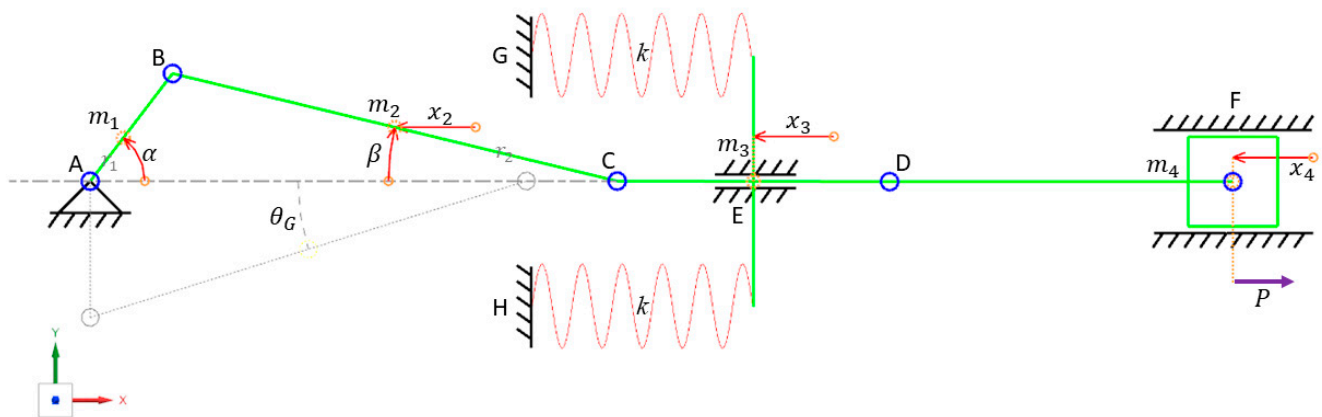
Figure 3. Body diagram of the piston compressor prototype.

By combining Equations (12) and (13), the expression for the slider (piston, push rod, and crosshead) displacement can be stated as Equation (15), and its velocity $\dot{x}$ is described in Equation (16)

$$x = l_1 - l_1 \cos \alpha + l_2 - \sqrt{l_2{}^2 - l_1{}^2 \sin^2 \alpha} \tag{15}$$

$$\dot{x} = \dot{\alpha} l_1 \sin \alpha + \frac{\dot{\alpha} l_1{}^2 \sin \alpha \cos \alpha}{\sqrt{l_2{}^2 - l_1{}^2 \sin^2 \alpha}} \tag{16}$$

Most occurring expression $\sqrt{l_2{}^2 - l_1{}^2 \sin^2 \alpha}$ could be stated as λ; hence, T is defined as (Equation (17))

$$T = \frac{1}{2} I_1 \dot{\alpha}^2 + \frac{1}{2} I_2 \left(\frac{\dot{\alpha} l_1 \cos \alpha}{\lambda} \right)^2 + \frac{M}{2} \left(\dot{\alpha} l_1 \sin \alpha + \frac{\dot{\alpha} l_1{}^2 \sin 2\alpha}{2\lambda} \right)^2 \tag{17}$$

The total potential energy of the system, V, is the sum of the potential energy of m_1 and m_2 due to their height, potential energy of the deformed springs, and external force from the air suction and compression process. So that

$$h_1 = r_1 + r_1 \sin \alpha \tag{18}$$

$$\theta_G = \arcsin \left(\frac{l_1}{l_2} \right) \tag{19}$$

$$h_2 = r_2 \frac{l_1}{l_2} (1 + \sin \alpha) \tag{20}$$

$$V = m_1 g h_1 + m_2 g h_2 + \frac{1}{2}(2k)x^2 + Px \tag{21}$$

$$V = m_1 g (r_1 + r_1 \sin \alpha) + m_2 g \left(r_2 \frac{l_1}{l_2} (1 + \sin \alpha) \right) + k(l_1 - l_1 \cos \alpha + l_2 - \lambda)^2 + P(l_1 - l_1 \cos \alpha + l_2 - \lambda) \tag{22}$$

Noted that the Lagrangian $\mathcal{L}$ is

$$\mathcal{L} = T - V \tag{23}$$

$$\mathcal{L} = \frac{1}{2} I_1 \dot{\alpha}^2 + \frac{1}{2} I_2 \left(\frac{\dot{\alpha} l_1 \cos \alpha}{\lambda} \right)^2 + \frac{M}{2} \left(\dot{\alpha} l_1 \sin \alpha + \frac{\dot{\alpha} l_1{}^2 \sin 2\alpha}{2\lambda} \right)^2 - m_1 g (r_1 + r_1 \sin \alpha) - m_2 g \left(r_2 \frac{l_1}{l_2} (1 + \sin \alpha) \right) \\ - k(l_1 - l_1 \cos \alpha + l_2 - \lambda)^2 - P(l_1 - l_1 \cos \alpha + l_2 - \lambda) \tag{24}$$

$$\frac{\partial \mathcal{L}}{\partial \alpha} = \frac{1}{2\lambda^4} I_2 \dot{\alpha}^2 l_1{}^2 \cos a \left(-2\lambda^2 \sin a + l_1{}^2 \sin 2\alpha \cos \alpha\right) + \frac{M l_1{}^2 \dot{\alpha}^2 \sin \alpha \left(l_2{}^2 \cos \alpha - \lambda l_1 \sin^2 \alpha\right)\left(\lambda + l_1 \cos \alpha\right)^2}{\lambda^4 - 2 l_2{}^2 l_1{}^2 \sin^2 \alpha}$$
$$- g \cos \alpha \left(m_1 r_1 + \frac{m_2 r_2 l_1}{l_2}\right) - \left(P + 2k(l_1 + l_2 - \lambda - l_1 \cos \alpha)\right)\left(\frac{l_1{}^2 \sin 2\alpha}{2\lambda} + l_1 \sin \alpha\right)$$
(25)

$$\frac{\partial \mathcal{L}}{\partial \dot{\alpha}} = I_1 \dot{\alpha} + \frac{1}{\lambda^2}\left(I_2 l_1{}^2 \dot{\alpha} \cos^2 \alpha + M \dot{\alpha} l_1{}^2 \sin^2 \alpha (\lambda + l_1 \cos \alpha)^2\right)$$
(26)

$$\frac{d}{dt}\left(\frac{\partial \mathcal{L}}{\partial \dot{\alpha}}\right) = I_1 \ddot{\alpha} + \frac{1}{\lambda^4}\ddot{\alpha} I_2 l_1{}^2 \sin 2\alpha + \frac{2}{\lambda^5}\ddot{\alpha} M l_1{}^2 \sin \alpha (\lambda + l_1 \cos \alpha)^2 \left(\lambda l_2{}^2 \cos \alpha + l_1{}^3 \sin^4 \alpha - l_2{}^2 l_1 \sin^2 \alpha\right)$$
(27)

As the joint frictions perform in the simulations, therefore Rayleigh's dissipation function $\mathcal{D}$ exists as stated in Equation (28) [28], so that the Lagrange equation with dissipation becomes as specified in Equation (29):

$$\mathcal{D} = \frac{1}{n+1}\sum_j c_j \dot{q}_j{}^{n+1}$$
(28)

$$\frac{d}{dt}\left(\frac{\partial \mathcal{L}}{\partial \dot{q}_j}\right) - \frac{\partial \mathcal{L}}{\partial q_j} + \frac{\partial \mathcal{D}}{\partial \dot{q}_j} = 0$$
(29)

In the simulations, phases that define the friction forces include stiction, transition, and dynamic since the piston (also the push rod and crosshead) have instantaneously zero velocity at the TDC and BDC. Depending on the piston position, the value of c_j in each joint is determined by the coefficient of static friction μ_s, coefficient of dynamic friction μ_d, and the absolute velocity threshold for the transition from dynamic friction to static friction. Frictions caused by normal forces within the bearings, crosshead-rail, and piston cylinder are proportional to the 0th power of velocity so that the dissipation functions related to the bearings in joint A, B, C, and crosshead-rail, as well as piston cylinder, are:

$$\mathcal{D} = 2c_b\left(\dot{\alpha} + \dot{\beta}\right) + \dot{x}\left(c_s + c_p\right)$$
(30)

$$\mathcal{D} = 2\dot{\alpha} c_b\left(1 + \frac{l_1 \cos \alpha}{\lambda}\right) + \dot{\alpha}\left(l_1 \sin \alpha + \frac{l_1{}^2 \sin 2\alpha}{2\lambda}\right)\left(c_s + c_p\right)$$
(31)

$$\frac{\partial \mathcal{D}}{\partial \dot{\alpha}} = 2c_b\left(\frac{l_1 \cos \alpha}{\lambda} + 1\right) + \left(\frac{l_1{}^2 \sin 2\alpha}{2\lambda} + l_1 \sin \alpha\right)\left(c_s + c_p\right)$$
(32)

By plugging all the terms, therefore, the general system's equation of motion can be expressed as (Equation (33))

$$\ddot{\alpha}\left[I_1 + \frac{1}{\lambda^4} I_2 l_1{}^2 \sin 2\alpha + \frac{2}{\lambda^5} M l_1{}^2 \sin \alpha (\lambda + l_1 \cos \alpha)^2 \left(\lambda l_2{}^2 \cos \alpha + l_1{}^3 \sin^4 \alpha - l_2{}^2 l_1 \sin^2 \alpha\right)\right]$$
$$- \dot{\alpha}^2\left[\frac{1}{2\lambda^4} I_2 l_1{}^2 \cos a\left(-2\lambda^2 \sin a + l_1{}^2 \sin 2\alpha \cos \alpha\right) + \frac{M l_1{}^2 \sin \alpha \left(l_2{}^2 \cos \alpha - \lambda l_1 \sin^2 \alpha\right)\left(\lambda + l_1 \cos \alpha\right)^2}{\lambda^4 - 2 l_2{}^2 l_1{}^2 \sin^2 \alpha}\right] + g \cos \alpha \left(m_1 r_1 + \frac{m_2 r_2 l_1}{l_2}\right)$$
$$+ \left[(P + 2k(l_1 + l_2 - \lambda - l_1 \cos \alpha)) + (c_s + c_p)\right]\left(\frac{l_1{}^2 \sin 2\alpha}{2\lambda} + l_1 \sin \alpha\right) + 2c_b\left(\frac{l_1 \cos \alpha}{\lambda} + 1\right) = 0$$
(33)

2.3. Physical Prototype

As shown in Figure 4, the physical prototype was built, resembling the MBD model, except for the drivetrain and spring attachment. In MBD simulations, only two extension-compression springs are mounted, while the physical prototype has 4 extension springs, as it is presented in Figure 4c. The prototype unit mainly consists of the compressor section and the electric drive section. Pulley and belt drivetrain are needed to multiply the available torque from the motor so that the lowest possible starting angular velocity is possible for the favorable slider sweep process. The level of external loads—that is, the magnitude of the air pressure—over the slider can be adjusted by the relief valve.
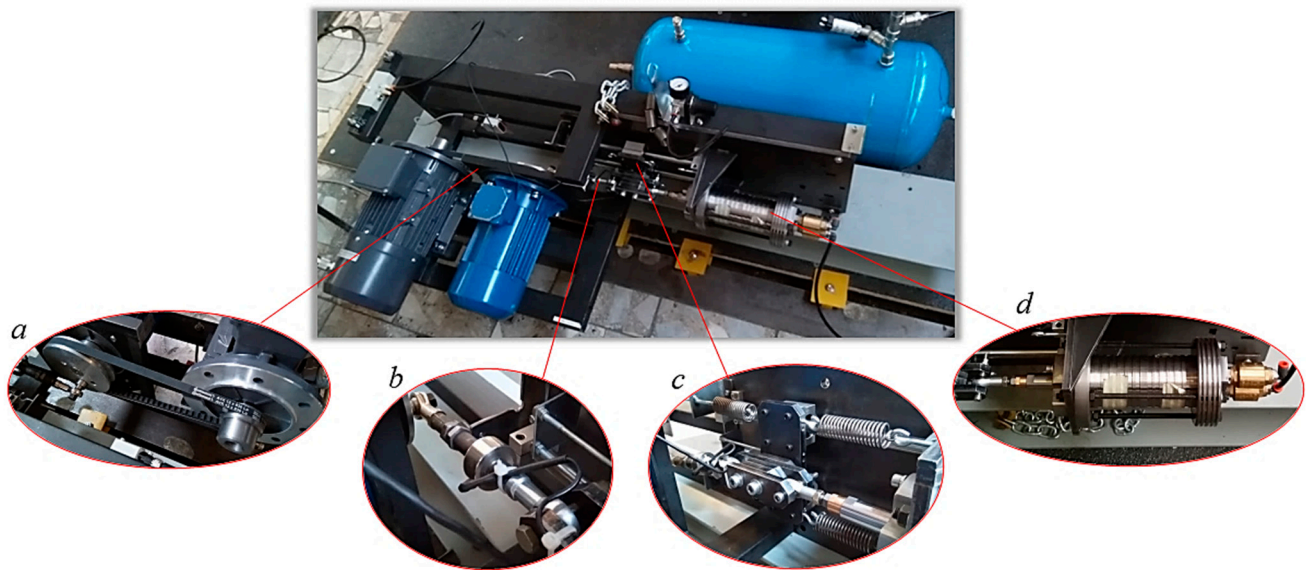
Figure 4. (**a**). Pulley and belt drivetrain, (**b**). force sensor on the connecting rod joint, (**c**). crosshead and springs, and (**d**). valves, cylinder, and piston connected to the crosshead.

Primarily, the electric drive system consists of a 3-phase motor, PLC, VFD, relay, circuit breaker, switches, cables, and control panel box. The assembled control unit in this system is programmed for the possibility of the motor to operate at a constant specified speed and steadily increasing speed (ramp function) to provide the sweep function to the slider. Hereinafter, the resonance speed of the system can be identified. Finally, setups with and without spring are tested to compare their forces in the connecting rod joints.

3. Results

3.1. Multi-Domain System Simulation Result

As described in Table 1, the initial position of the crank is set to 0°, which means that the piston is initially located at TDC. The cycle starts from the suction stroke, TDC to BDC (0° to 180° of crank); followed by the compression stroke, BDC to TDC (180° to 360° of crank). The compressed air is accumulated inside the tank, and the pressure gradually builds up until reaching the relief valve cracking pressure. As depicted in Figure 5a,b, by setting the relief valve cracking pressure at 8.7 bar, for instance, the maximum pressure achieved inside the cylinder $p_{l_{max}}$ is about 8.84 bar, and the force pushing down the piston reaches around 2500 N.

Figure 5b shows the force–crank angle curve in one cycle. To await pressure build-up as the tank is filled up, which takes place for the first 0.85 s (in Figure 5a), the crank angle from 14,400° to 14,760° is taken for the plot so that the expected steady load upon the piston is achieved. Within one cycle, there are several stages that take place. At BDC, point 'd', the cylinder is already filled with the air after suction as the piston moves from TDC to BDC, and the inlet valve opens at point 'c' to 'd'. When the piston moves toward TDC, from 'd' to 'e', the air is compressed, and the pressure so does the force upon the piston, rises up until the outlet check valve opens at point 'e'. Discharge occurs from point 'e' to 'a', and between 'a' and 'b', there is left-over pressure inside the cylinder before the outlet valve is finally closed at 'b', and so the piston displacement from 'b' to 'c' is only expansion without having any valve open. Several simulations in Amesim are performed to generate the data of force in the example case of 2.5, 5, 7.5, and 10 bar of air pressure. Based on these simulations, the data of force upon the piston F_l versus angular position of crank modulo 360 are imported to ADAMS/View as a spline. This spline is used as the input value of applied force, which is placed at the top of the piston as the function of crank angle in the MBD model.
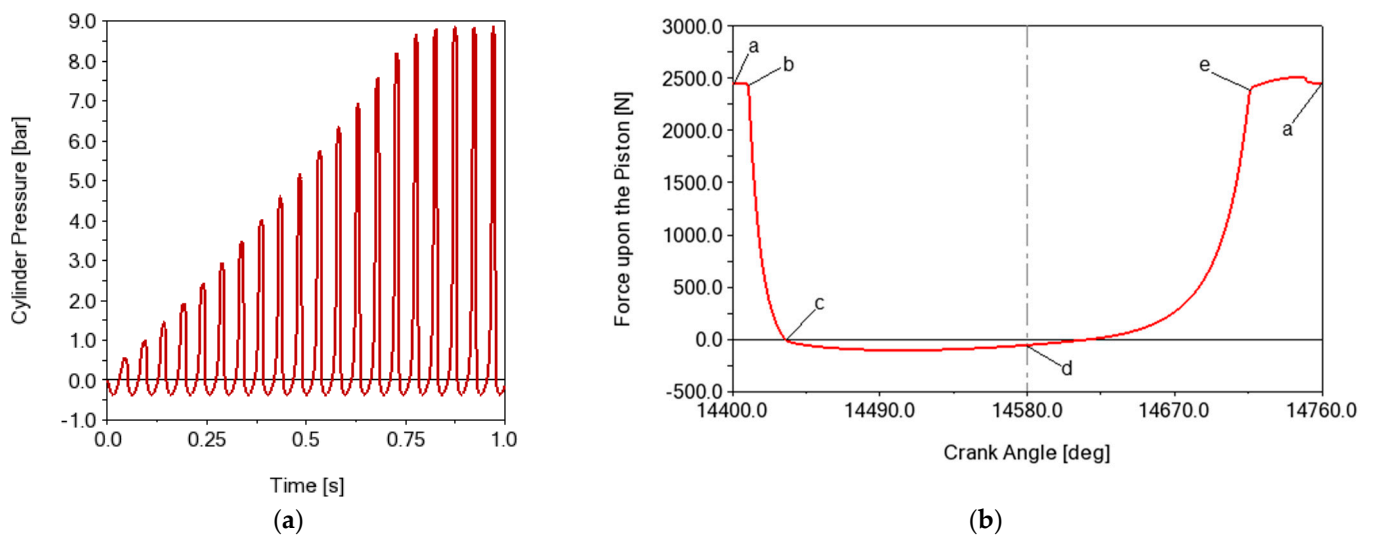
(**a**)　　　　　　　　　　　　　　　　　　　　　　　(**b**)

Figure 5. (**a**). Air pressure inside the cylinder as the tank is filled up, and (**b**). force acting on the piston in one cycle (0° to 360° of crank); the process consists of expansion (a–c), effective suction (c–d), compression (d–e), and discharge (e–a).

3.2. Multibody Dynamics Simulation Result

This subsection describes the effect of resonance application in the system's dynamics by performing effort estimation of two main setups: 1. without spring and 2. with spring. In MBD simulation, effort estimation is performed by measuring the power required for the rotational motion generator to accelerate a known mass, whatever force is required to make the part satisfy the motion. The principle is equivalent to the "inertia" dynamometer, which provides a fixed inertial mass load, calculates the power required to accelerate that fixed and known mass, and records the angular velocity and acceleration rate to calculate torque.

3.2.1. Elementary Comparison

To observe what is the maximum possible reduction of torque between two different setups, no dissipative forces are included in this section of comparison. The parameter for the simulation is set to the values shown in Figure 6's description. In the setup with spring, an equilibrium position is attained in which the crank angle is not exactly at 270° as in the case of the setup without spring. It is important that at the equilibrium after the springs are installed, the reciprocating masses should be in the middle of its stroke; otherwise, resonance would not be achieved.
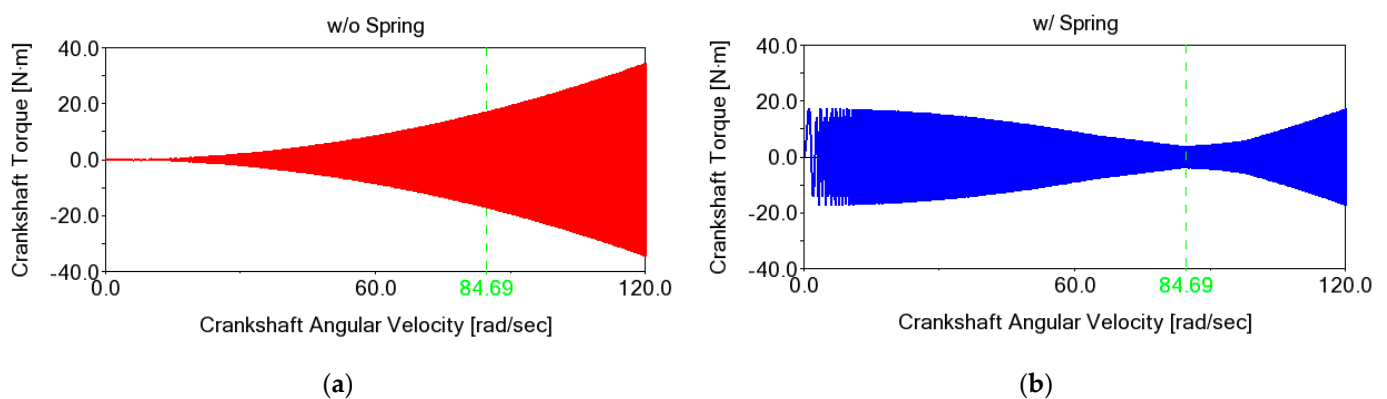

(**a**)　　　　　　　　　　　　　　　　　　　　　　　(**b**)

Figure 6. Torque–angular velocity curves: (**a**). without spring, (**b**). with spring; M = 1.5 kg, k = 6.25 kN/m.

Figure 6a shows that the setup without spring has a progressive increment of the dynamic torque as the angular velocity increases. On the other hand, the setup in which the springs are installed (Figure 6b) has a lower magnitude of dynamic torque at its resonant frequency of around 84.69 rad/s. In this second case, at the resonant frequency, the system effectively stores and transfers energy between the kinetic energy of the slider and the potential energy of the spring so that the torque (that is, the required effort) for the crankshaft to rotate is significantly lower than in any other angular velocity. The resonant frequency ω_r, in this case, is not the same as the natural frequency ω_0—in which, if calculated by $\sqrt{k/m}$, is 91.28 rad/s—since the slider-crank mechanism exhibits periodic but non-harmonic motion of the slider. It is also worth mentioning that the magnitude of the torque, at each instant of crank angle, is proportional to the mass of reciprocating components M, crank radius l_1, and crankshaft angular velocity ω; and it is inversely proportional to the length of connecting rod l_2.

From the front view of the model (Figure 3), it shall be noted that any quantity aiming in the counterclockwise direction has a positive value; otherwise, it is negative. Figure 7a shows that at a constant angular velocity of 84.69 rad/s, which is the resonant frequency, positive and negative values of torque (counterclockwise and clockwise) are involved within one cycle. In the setup without spring, crank displacement from 0° to about 74° results in negative values of torque since the reciprocating mass M is being accelerated from its instantaneous rest ($\dot{x} = 0$) at TDC up to about the middle of the stroke. As the motion generator rotates the crank at a constant velocity, it "receives" positive values of torque as M is being decelerated from 74° up until it instantaneously rests at 180° (BDC). These processes continue in a similar way, yet in opposite magnitude and order, when the crank is displaced from 180° to 360°. In sum, the energy transferred and received by the rotational joint motion generator is conserved, i.e., positive plus negative values of the work performed are zero.
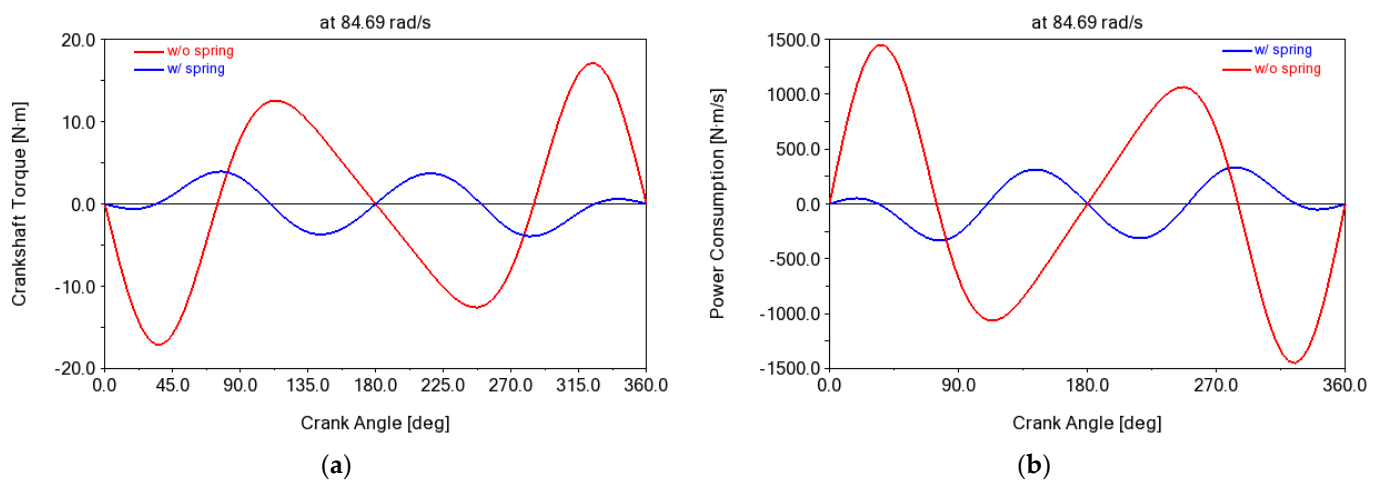

Figure 7. Torque–crank angle (**a**) and power–crank angle (**b**) curves within one cycle at resonant frequency $\omega_r = 84.69$ rad/s. Red line, setup without spring; blue line, setup with spring.

Nonetheless, in reality, the model with higher dynamic torque will have the drawbacks of having higher stresses in the components, higher joint frictions, and higher demand for driving power, which might likely result in higher dissipation of energy. In the setup with spring at resonance, it can be seen in Figure 7a that it has three crests and three troughs of dynamic torque, and their magnitudes are significantly lower than the conventional setup. At the brief displacement from 0° to about 33°, there are negative values of dynamic torque, which is much smaller because the previously extended spring is pulling the reciprocating mass M, "helping" the motion generator to accelerate the mass M. As the magnitude of counterclockwise torque due to the spring force along with the inertial force of reciprocating mass overlaps the amount of torque needed to accelerate the reciprocating mass from 33°

to 108°, the torque becomes positive. Crank displacement continues from 108° to 180° in which the springs are being compressed so that the torque in this interval is negative. Processes similarly continue in opposite order and magnitude when the crank rotates from 180° to 360°. Likewise, in this setup, the total work performed within one cycle is zero; energy is conserved.

Furthermore, as shown in Figure 7b, it can be pointed out that the power consumption (the amount of energy transferred out from the motion generator to the system per unit time, or the product of torque and angular velocity) is positive when the value of torque is negative (clockwise direction). Figure 8 presents the plots of power consumption over the angular velocity, displayed only on the positive values representing the magnitude of power demand for the system to operate. The setup with spring, Figure 8b, shows that at a resonant frequency, the magnitude of power demand is about 0.3 kW, unlike the conventional one, which might require power at around 1.4 kW. The negative value of power—which is shown in Figure 7b but is not portrayed in Figure 8—indicates that the motion generator is "receiving" power due to the inertial torque described earlier. To wrap up, it can be stated that the advantageous manner to run the slider-crank system is at the resonant frequency, possibly by adding the element that can store and transfer the potential energy from the reciprocating mass's kinetic energy so that the equilibrium position of its reciprocating mass is at the middle of its stroke.
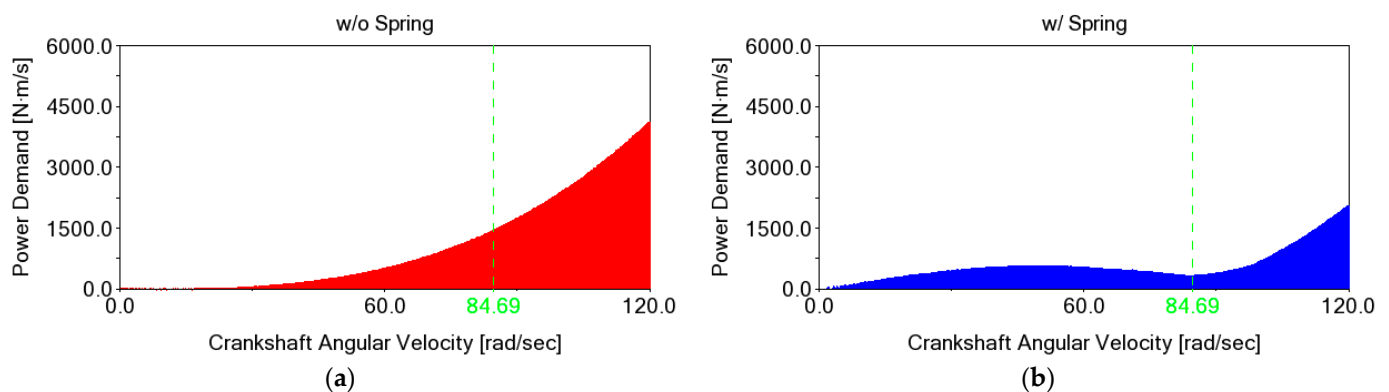

Figure 8. Power demand–angular velocity curves; (**a**). without spring, (**b**). with spring.

3.2.2. Influence of the Frictional Forces

In reality, there are some energy losses from cycle to cycle caused by damping. Coulomb damping, a type of mechanical damping in which energy is dissipated through sliding friction, is the major concern in the analyzed models. This subsection compares the setup with spring at resonance in 3 coefficient of friction scenarios (shown in Table 3) to observe if the utilization of resonance is still applicable in a more realistic case. Friction case 2 is based on the following reference: cylindrical joint of piston cylinder [29,30]; translational joint of crosshead-rail, default in ADAMS/View; revolute joint of deep groove ball bearing [31,32]; while friction case 3 is based on the two-fold value of μ_d of friction case 2.

Table 3. Coefficient of frictions for the compared setups; $M = 1.5$ kg, $k = 6.25$ kN/m, $\omega_r = 84.69$ rad/s.

Friction Case	Cylindrical Joint (F)		Translational Joint (E)		Revolute Joint (A, B, C, and D)	
	μ_s	μ_d	μ_s	μ_d	μ_s	μ_d
1	0	0	0	0	0	0
2	0.035	0.03	0.004	0.002	0.0015	0.001
3	0.065	0.06	0.006	0.004	0.0025	0.002

Figure 9a compares different friction scenarios when all are run with spring in resonance. As depicted in the plot, a higher coefficient of friction will drop the curve into a lower position. In the setup where the frictions are inexistent (friction case 1), as previously explained in Section 3.2.1, the sum of the dynamic torque within one cycle is zero; the energy is conserved. Friction case 2 results in −0.4 N·m of average dynamic torque, while case 3 has −0.8 N·m; these will result in energy consumption of 2.51 and 5.02 J/cycle, respectively. Nevertheless, it can be observed in Figure 9b that the setup with spring in resonance still has significantly lower dynamic torque compared to the setup without spring. In the setup without spring, curves in dash line, friction case 2 has −1.04 N·m average dynamic torque, while case 3 has −2.08 N·m; these will end in energy consumption of 6.53 and 13.07 J/cycle, respectively. Overall, when there is no external load and only friction is involved, the percentage of energy saving by the use of resonance in the presented model is around 61.6% for both friction cases 2 and 3.
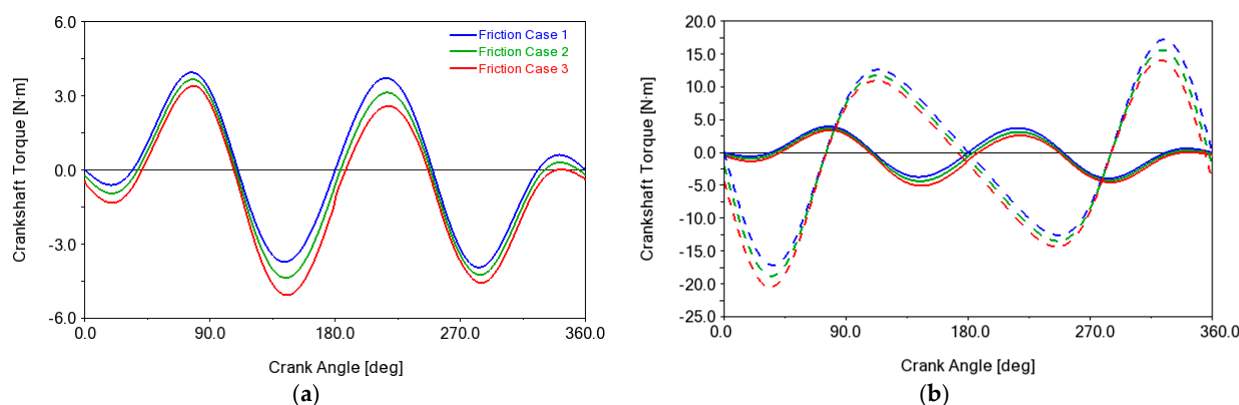

Figure 9. Torque–crank angle curves within one revolution of the crankshaft at resonance (84.69 rad/s); (**a**). setup with spring attached at resonance at different frictions, (**b**). comparison of the setup with spring at resonance (solid line) and the setup without spring (dash line) at different frictions.

3.2.3. Influence of the Pressure Loads: Suction and Compression Forces in the Work of Compressor

This subsection presents the effectiveness of resonance application in slider-crank mechanism loaded by different values of external forces. In MBD simulations, force at the top of the piston as the external load is put by employing single-component applied force with Akima Fitting Method as its input function. This runtime function consists of the modulo operation of crank angle as the independent variable and the previously imported spline data of force from Simcenter Amesim, similarly as shown in Figure 5b, as the dependent variable. In ADAMS/View, the syntax of the runtime function of the Akima Fitting Method is written in the form of

AKISPL(1st_Indep_Var, 2nd_Indep_Var, Spline_Name, Deriv_Order)

while the function measure is written in

MOD(x1, x2).

Independent variable is only put in 1st_Indep_Var of the AKISPL function, and the spline name is set to the name of spline based on which magnitude of the force the model would like to be tested, while the derivative order is set to be 0. The function measure of MOD is always set to the same value: cumulative measure of the crank angle in x1, and 360 (that is, one revolution or one cycle) is put in x2.

Figures 10 and 11 show the simulation results based on the setup defined in Table 4. Figure 10c compares the situation in which the setup with spring is run at resonance, and the setup without spring (which in the reciprocating compressor is conventionally run at an arbitrary speed depending on the prime mover and flow rate demand) is run at those same angular frequency denoted by the green line in Figure 10a,b. It can be observed that when the motion generator is operated at those resonant frequencies, the crankshaft RMS

torque and motion generator power consumption of the setup with spring is noticeably lower. Nonetheless, not only the setup with spring, it can be observed that the setup without spring also has a narrow torque region around its own resonant frequency since the compression of the air itself acts as a spring compression. In this practical example, air compression can also be utilized to provide resonance. Based on the following simulations, if the setup without spring is run at its own resonant frequency, no significant difference in RMS torque and motion generator power consumption can be noticed when it is compared with the setup with spring run at its own resonant frequency. In the case of working with a system that has adjustable prime mover angular velocity, if the resonance has been achieved at its own compression load, spring might not be needed, and resonance can still be attained; otherwise, installation of spring with different stiffness might be used to change the resonance frequency to match with the available prime mover angular velocity. In detail, the essential data obtained from both Figures 10 and 11 are shown in Table 4.

3.2.4. Influence of the Reciprocating Masses

This subsection describes the comparison of the setup with and without spring using three different reciprocating masses at the angular velocities in which the setup with spring achieves resonance. As stated in Table 5, friction and load cases are set to the same values for all setups. All of the setups are also using the same spring stiffness, and as a result, distinct masses will specify their own resonant frequencies. As indicated by the blue curves of Figure 12, due to the use of similar spring stiffness, the reciprocating masses and their matching resonant frequencies will generate the same magnitude of inertial force. As a result, as shown in Table 5 and Figure 13, the RMS torque and the percentage decrease in power consumption are also practically similar. Table 5 also shows that higher mass requires lower average power consumption at the comparable value of load since the higher mass defines lower resonant frequency compared to the lighter mass in case both are using the same spring stiffness. In Figure 13, it can be observed that the curves are digressive as the compression load is getting closer to zero, and they are practically linear as the compression load goes higher.

3.2.5. Influence of the Crankshaft Angular Velocity (Using Different Spring Stiffnesses)

In this subsection, a comparison of the setup with and without spring using three distinct spring stiffnesses with the same reciprocating mass is described. For all setups in comparison, friction cases and external load cases are set to equal values. Since all of the setups use equal mass, different spring stiffness will entail a different angular velocity ω_r to attain resonance. In this particular case, different angular velocities will determine the different magnitudes of inertial forces, as it is shown by the red curves in Figure 12. As a result, as it is shown in Table 6 and Figure 14, the RMS torque and the percentage decrease in power consumption are significantly higher as the spring stiffness attached is set to a higher value. Likewise, in Figure 14, it can be noticed that the curves are digressive as the compression load gets closer to zero but linear as the compression load goes higher.

Table 4. Comparison of the setup with and without spring; M = 3 kg, k = 6.25 kN/m, friction case 2.

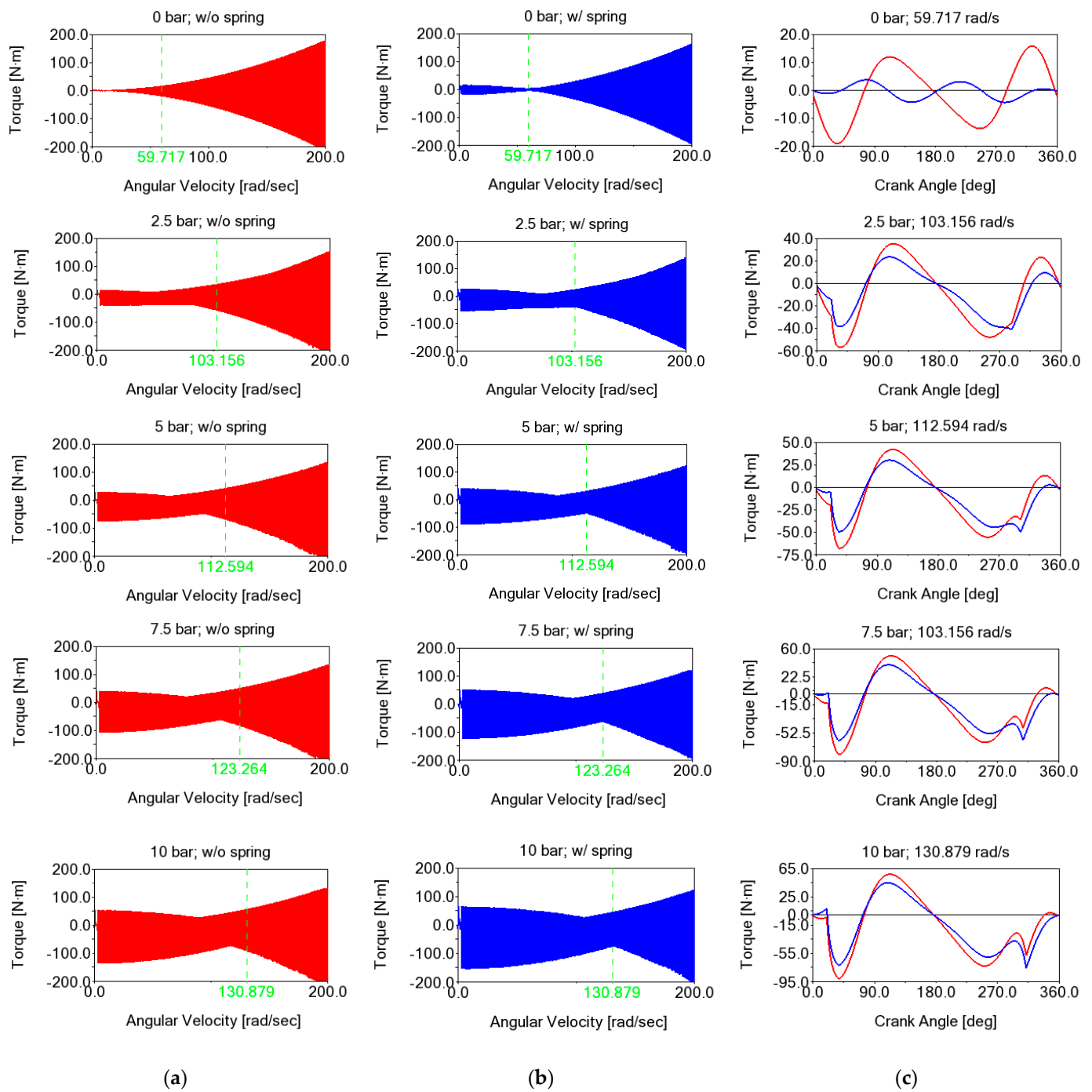| Load F_l (bar)	ω_r (rad/s)	τ_{RMS} (N·m)		P_{avg} (N·m/s)		Decrease in P_{avg} (%)
		w/o Spring	w/Spring	w/o Spring	w/Spring	
0	59.717	10.39	2.44	303.86	72.51	76.14
2.5	103.156	29.99	21.48	1820.22	1340.84	26.34
5	112.594	34.34	27.14	2355.49	1917.79	18.58
7.5	123.264	40.45	33.71	3062.98	2646.66	13.59
10	130.879	44.94	38.63	3614.31	3261.74	9.75

Figure 10. Torque–angular velocity curves (**a**,**b**) and torque–crank angle curves within one cycle at resonant frequency (**c**), loaded with different values of external forces. Red, setup without spring, and blue, setup with spring.
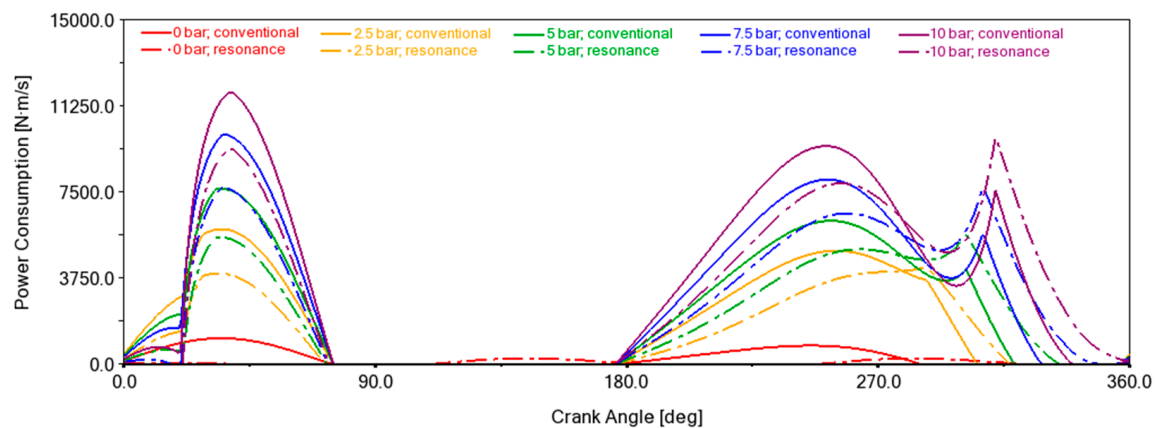
Figure 11. Power consumption–crank angle curves within one cycle at the resonant frequency of the setup with spring, loaded with different values of external forces.

Table 5. Comparison of the setup with and without spring; k = 6.25 kN/m, friction case 2.

| Load F_l (bar)	ω_r (rad/s)	τ_{RMS} (N·m)		P_{avg} (N·m/s)		Decrease in P_{avg} (%)
		w/o spring	w/spring	w/o spring	w/spring	
M = 1.5 kg						
0	86.09	10.59	2.37	446.87	102.27	77.12
2.5	147.35	29.99	21.47	2602.0	1917.39	26.31
5	159.12	33.75	26.70	3285.52	2677.51	18.51
7.5	173.84	39.63	33.11	4251.46	3687.2	13.27
10	184.16	43.94	37.93	5006.36	4538.68	9.34
M = 3 kg						
0	59.717	10.39	2.44	303.86	72.51	76.14
2.5	103.156	29.99	21.48	1820.22	1340.84	26.34
5	112.594	34.34	27.14	2355.49	1917.79	18.58
7.5	123.264	40.45	33.71	3062.98	2646.66	13.59
10	130.879	44.94	38.63	3614.31	3261.74	9.75
M = 4.5 kg						
0	48.45	10.33	2.47	245.05	59.76	75.62
2.5	84.47	30.35	21.78	1506.34	1111.92	26.18
5	89.94	33.29	26.39	1835.07	1495.63	18.49
7.5	99.58	39.98	33.38	2452.64	2122.91	13.44
10	107.47	45.59	39.11	3000.48	2700.02	10.01
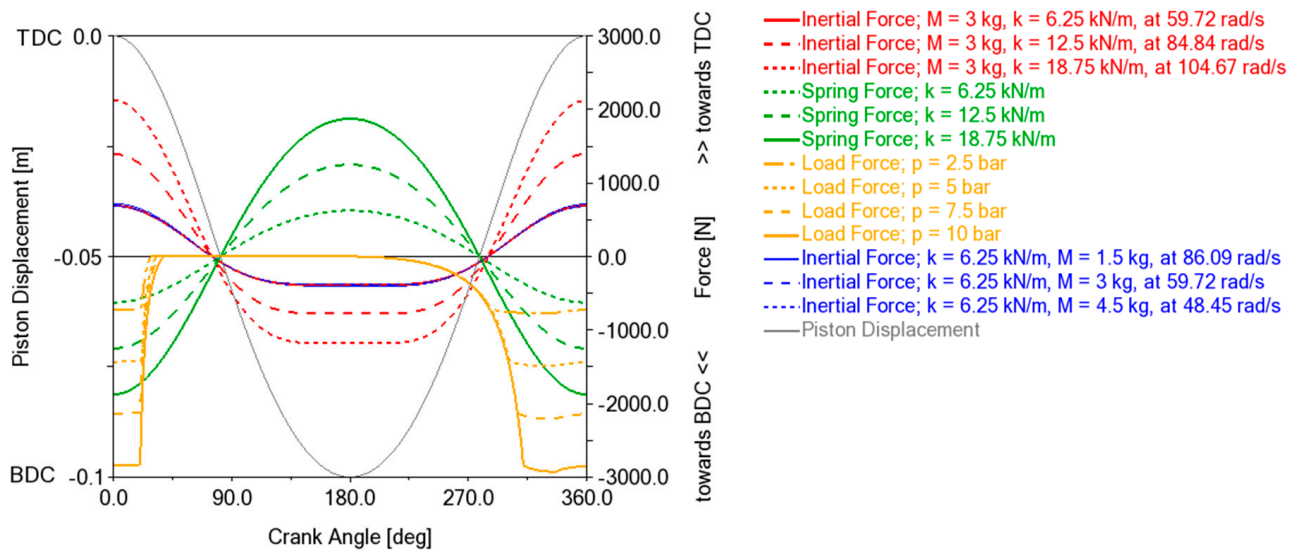
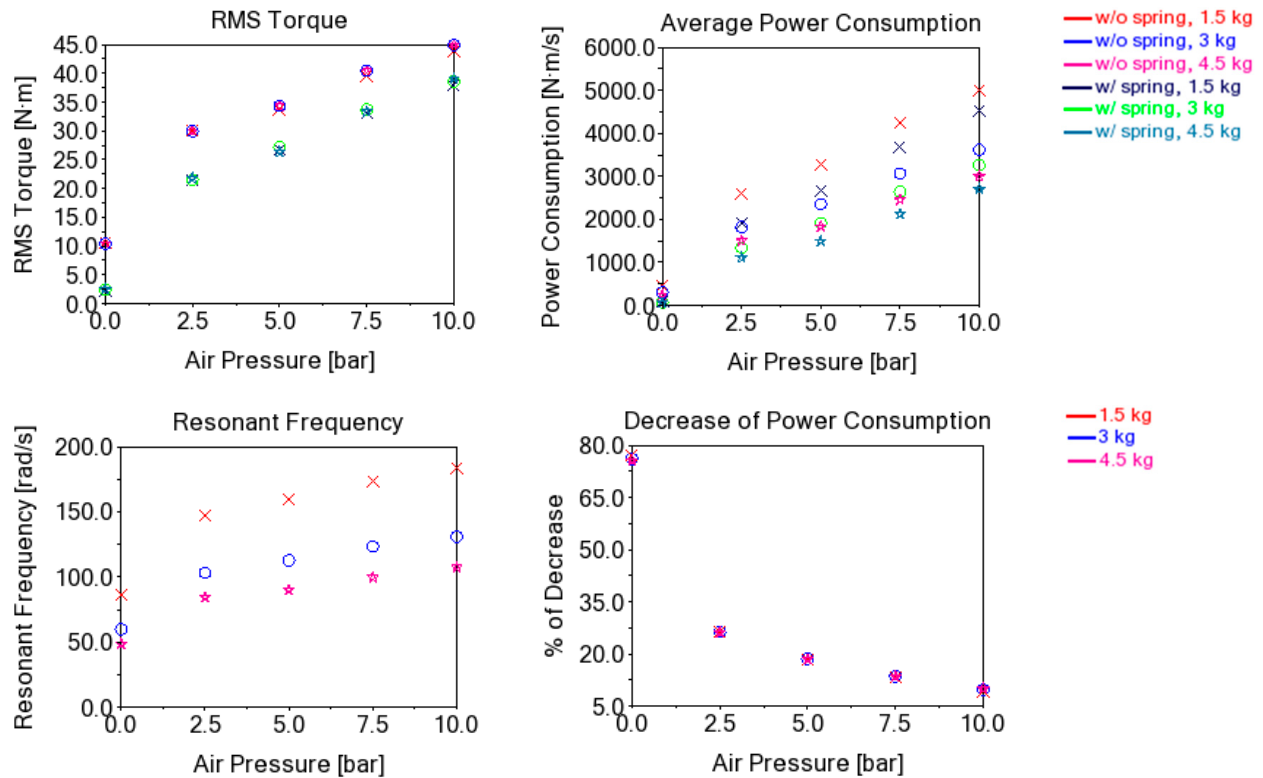**Figure 12.** Involved forces in one revolution of the crankshaft.

Figure 13. Comparison of the setup with and without spring over 3 different reciprocating masses; k = 6.25 kN/m, friction case 2.

Table 6. Comparison of the power efficiency for setup with and without spring; M = 3 kg, friction case 2.

k = 6.25 kN/m						
Load F_l (bar)	ω_r (rad/s)	τ_{RMS} (N·m)		P_{avg} (N·m/s)		Decrease in P_{avg} (%)
		w/o spring	w/spring	w/o spring	w/spring	
0	59.717	10.39	2.44	303.86	72.51	76.14
2.5	103.156	29.99	21.48	1820.22	1340.84	26.34
5	112.594	34.34	27.14	2355.49	1917.79	18.58
7.5	123.264	40.45	33.71	3062.98	2646.66	13.59
10	130.879	44.94	38.63	3614.31	3261.74	9.75
k = 12.5 kN/m						
Load F_l (bar)	ω_r (rad/s)	τ_{RMS} (N·m)		P_{avg} (N·m/s)		Decrease in P_{avg} (%)
		w/o spring	w/spring	w/o spring	w/spring	
0	84.84	20.99	4.83	871.67	202.04	76.82
2.5	120.15	40.21	22.49	2738.47	1591.85	41.87
5	125.67	41.95	26.90	3107.26	2086.52	32.85
7.5	136.38	48.28	33.75	3896.65	2897.98	25.63
10	144.12	52.92	38.92	4494.54	3580.94	20.33
k = 18.75 kN/m						
Load F_l (bar)	ω_r (rad/s)	τ_{RMS} (N·m)		P_{avg} (N·m/s)		Decrease in P_{avg} (%)
		w/o spring	w/spring	w/o spring	w/spring	
0	104.67	31.95	7.17	1636.63	372.08	77.27
2.5	136.78	52.09	24.63	3923.47	1924.65	50.95
5	142.86	54.08	29.19	4385.18	2509.96	42.76
7.5	150.36	58.39	34.86	5024.43	3242.02	35.47
10	157.09	62.44	39.69	5580.87	3914.79	29.85

The selection of proper stiffness in relation to achieving the resonance conditions is possible based on the dynamic system simulation method presented in this paper. Equivalent spring stiffness is defined as:

$$k_e = k_s + k_g \tag{34}$$

where

k_s—mechanical spring stiffness;

k_g—gas spring stiffness.

Depending on the required RPM of the electric motor (constant/variable), the equivalent spring stiffness can be obtained in the following way:

- For low-speed compressors, only gas spring can be used depending on the discharge pressure range.
- For high-speed compressors, an additional steel spring set can be used to achieve the resonance conditions.

The use of constant-speed motors requires a relatively exact selection of the equivalent stiffness in the compressor. By variable speed drives (VSD), the resonance conditions can be achieved using, i.e., the appropriate frequency tracking control system [33].
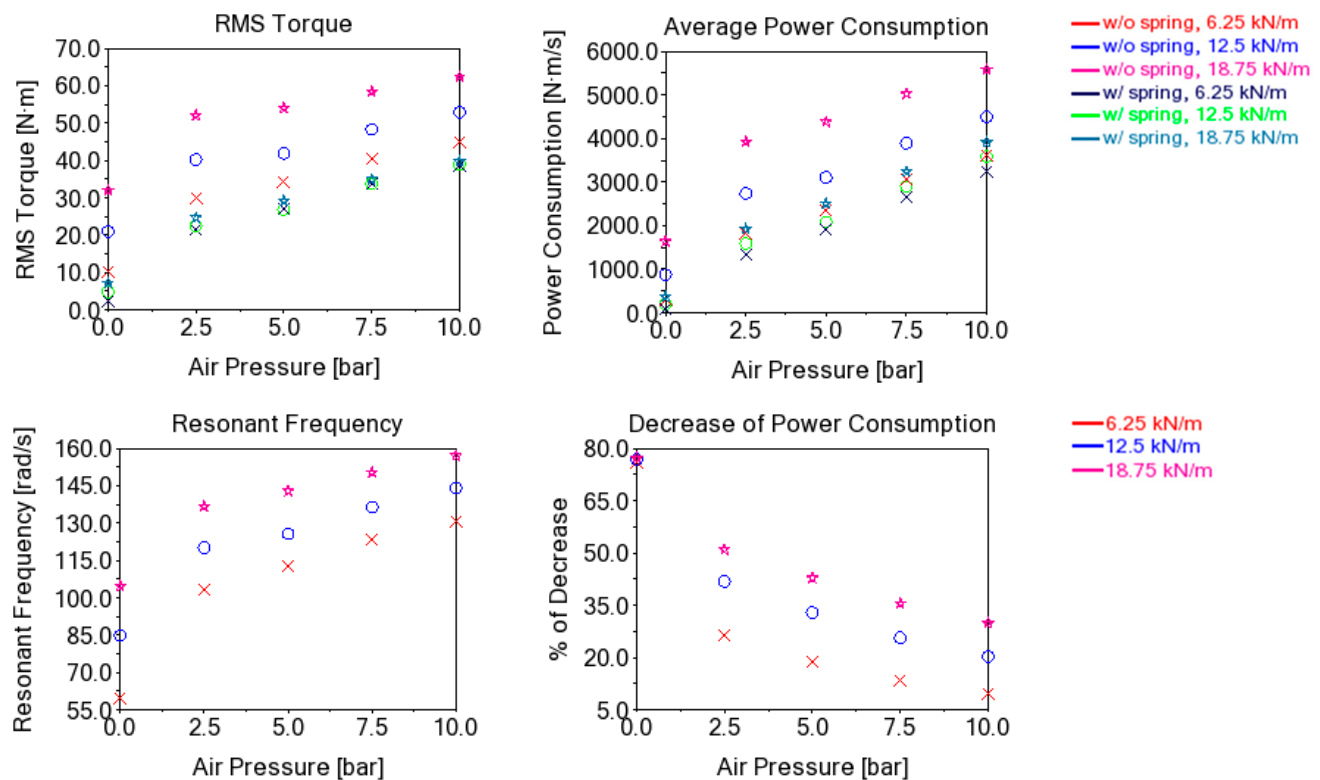
Figure 14. Comparison of the setup with and without spring over 3 different spring stiffnesses; *M* = 3 kg, friction case 2.

3.2.6. Forces on Joints

Forces on joints determine the developed heat and material wear due to the generated frictions, and hence particularly important to be considered in the design and material selection of joint bearings. In this subsection, component connection joint forces in the setup with and without spring are compared. The simulation setup and essential results are described in Table 7, and the entire results are shown in Figure 15. It can be observed that all rotating joints—that is, crankshaft to the main frame, connecting rod to crankshaft, and crosshead to connecting rod—of the setup with spring at resonance have many times lower peak and RMS value of force. This behavior can also be observed for the slider-crank mechanism with a load, but the impact of resonance depends on the relation between the value of inertial force to the gas pressure force. If the pressure force is many times higher than the inertia force, the impact of resonance will be smaller.

3.3. *Physical Prototype Experimental Result*

Due to the capability limitation, the physical prototype is only tested with up to 1 bar of air pressure. Testing results are shown in Figure 16, and their essential data are presented in Table 8. It can be observed that all setups with spring have narrow force regions around resonance speed. Nearly the same as the simulation, setup with spring provides about a 60.34% reduction of peak-to-peak force at resonance when no pressure load is involved (and no valves are installed). Attachment of the valves even poses as an external load so that peak-to-peak force is reduced by only 20.9%. This result underlines the important role of the pressure losses occurring at the inlet and outlet valves in order to obtain the highest positive resonance effect.

Table 7. Comparison of the setup with and without spring based on the simplified model presented in Figure 3; M = 3 kg, k = 6.25 kN/m, ω_r = 43.3 rad/s, F_l = 0 bar, friction case 1, joint designation refers to Figure 3.

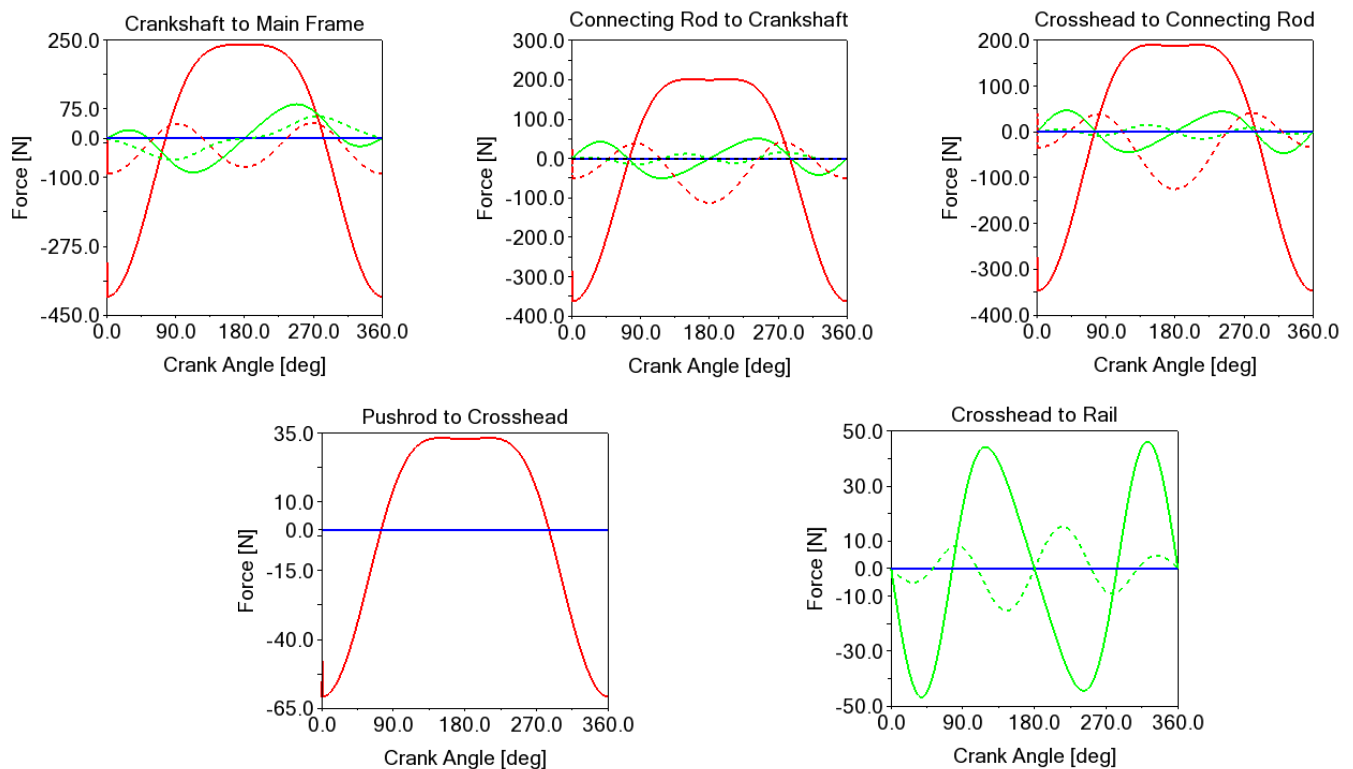| Joint	Connection	F_{RMS_x} (N)		F_{RMS_y} (N)	
		w/o Spring	w/Spring	w/o Spring	w/Spring
A	Crankshaft to main frame	234.66	48.74	50.39	32.95
B	Connecting rod to crankshaft	207.44	53.19	33.01	8.06
C	Crosshead to connecting rod	197.49	56.96	31.61	7.81
D	Push rod to crosshead	34.65	34.65	0	0
E	Crosshead to rail	0	0	31.61	7.81

Figure 15. Comparison of joint forces in the setup without spring (solid line) and the setup with spring (dash line) based on the simplified model presented in Figure 3. Red, *x* axis; green, *y* axis; blue, *z* axis.

As is demonstrated in the simulations, the compression of air itself takes effect as a spring compression. Even without any steel spring installed, a narrow force region can be observed in the setup without spring. At 1 bar compression load, the reduction of force goes down to 6.26% and 16.24% at 126.4 rad/s and 141.8 rad/s, which are the resonance speed of both setup without spring and setup with spring, respectively. Nonetheless, if both setups are run and compared at their own resonant speed—that is, 126.4 rad/s for the conventional setup and 141.8 rads for the resonance setup—the difference of peak-to-peak force is less significant; only about 1.53%. Therefore, in the process of air compression, the spring might or might not be installed depending on the available system's parameters. As

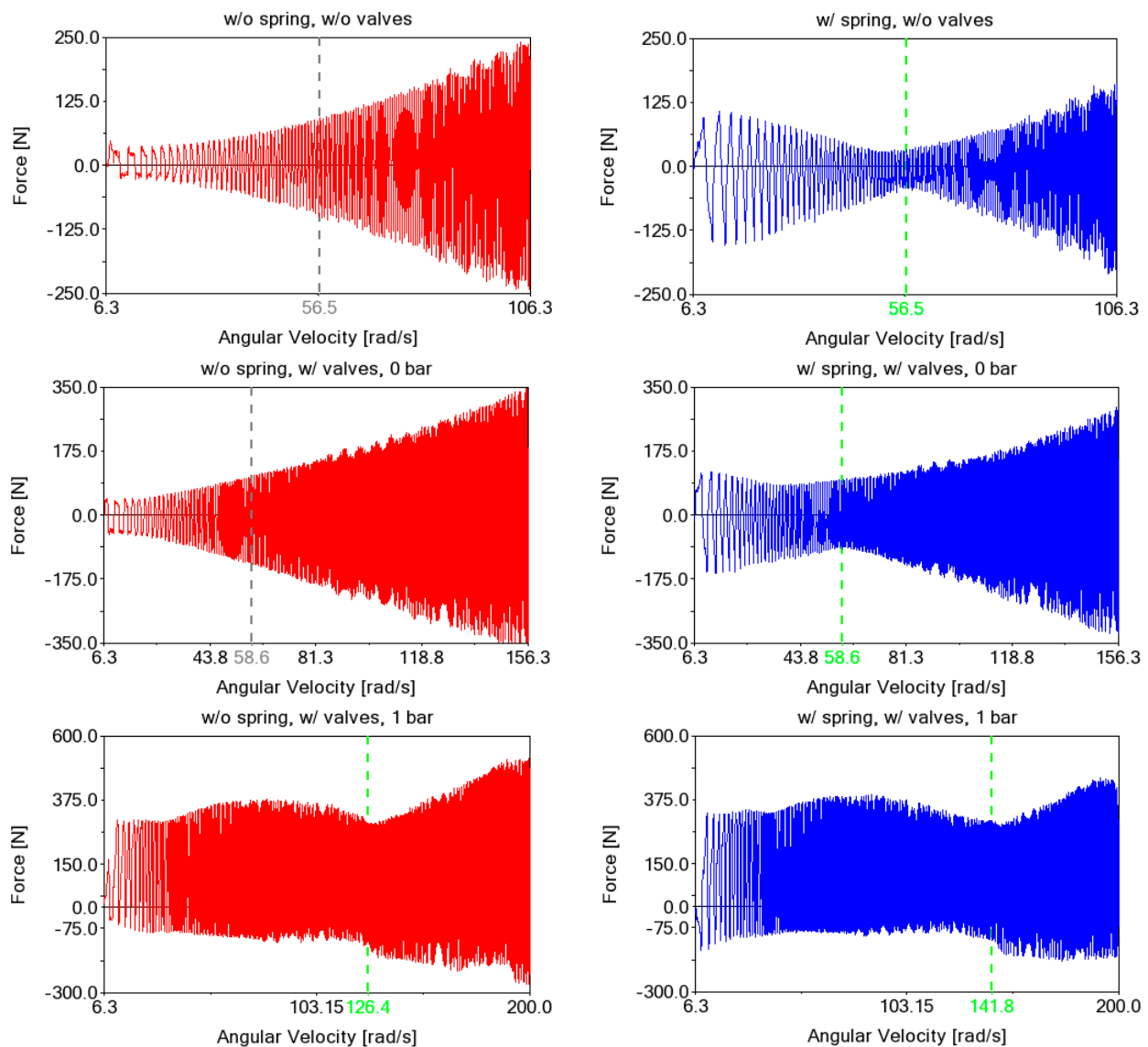long as the system is run at a resonant frequency, enhancement of the system's dynamics might be achieved.

Figure 16. Force–angular velocity curves. Force is measured on the connecting rod, as shown in Figure 4b. Red curves: without spring, blue curves: with spring; M = 3.9 kg, k_{eq} = 2.5 kN/m.

Table 8. Comparison of the generated force on the connecting rod of the physical prototype; M = 3.9 kg, k_{eq} = 2.5 kN/m.

Load F_l (Bar)	Resonance Speed ω_r (rad/s)	Pulling Force F_{min} (N)		Pushing Force F_{max} (N)		Peak-to-Peak Amplitude of Force F_{pp} (N)		Decrease in Peak-to-Peak Amplitude of Force (%)
		w/o Spring	w/Spring	w/o Spring	w/Spring	w/o Spring	w/Spring	
w/o valves	56.5	−99.84	−43.92	93.2	32.64	193.04	76.56	60.34
0	58.6	−134.64	−92.08	106.08	98.32	240.72	190.4	20.90
1	126.4	−133.28	−84.08	295.04	317.44	428.32	401.52	6.26
1	141.8	−181.68	−121.04	321.84	300.72	503.52	421.76	16.24

4. Conclusions

In this article, a technique for improving the slider-crank mechanism dynamics using the phenomenon of mechanical resonance is presented. Comparative study toward the resonance and conventional operation is performed using multibody dynamics (MBD) simulation and experimental investigation. As the practical case study example, a reciprocating compressor model is explored, representing the application of a slider-crank mechanism.

At first, the CAD model is prepared and simulated in MSC ADAMS. To simulate the dynamics of fluid, an equivalent multi-domain system of the model is also made in Simcenter Amesim. Comparisons are performed in two main operation setups: 1. without spring; and 2. with spring; both are set in comparable component specifications and constraints. System performance is analyzed by investigating the joint forces, dynamic torque, and estimated power demand of both two main setups within 78 different scenarios of simulation; that is, resulting from different configurations of friction, pressure load, reciprocating mass, and spring stiffnesses.

In the condition where the dissipative forces are inexistent, both the conventional and the resonance slider-crank setup have zero total work performed within one cycle. Even so, the resonance setup has the advantage of having significantly lower dynamic torque amplitude compared to the conventional one, basically due to the compensation of inertial forces by spring forces and this occurs without use counterweights. Coulomb damping is the major cause of energy dissipation in the system. A higher coefficient of friction will drop the torque–crank angle curve into the lower position, which means that the energy being dissipated per cycle is larger. It is found that the setup without spring also presents a narrow torque region around resonant frequency since the process of air compression itself acts as a spring compression. Whether or not the system uses the spring, as long as it is run at the resonant frequency, the advantageous result of resonance utilization can be achieved. On the equivalent spring stiffness, distinct masses will specify their own resonant frequencies. Different reciprocating masses and their matching resonant frequencies will generate the same magnitude of the inertial force of the reciprocating mass since the spring stiffness is identical, resulting in practically similar RMS torque. Because the higher mass defines lower resonant frequency compared to the smaller mass in case both are using the same spring stiffness, the system with higher reciprocating mass is favorable since it requires lower average power consumption to deal with the comparable value of the load. Different resonant frequencies will determine the different magnitude of inertial forces of the reciprocating mass, and as a result, the RMS torque is notably higher as the spring stiffness attached is set to a higher value. From the simulation results presented in Table 6, it can be seen that increasing the equivalent spring stiffness (air spring plus steel spring) leads to higher power efficiency. All rotating joints of the setup with spring at resonance have lower peaks and RMS value of force on joints.

Finally, experimental verification of the slider-crank mechanism at resonance demonstrates equivalent behavior with the simulations. Not only by the use of steel spring, in the case of the work of a compressor system, resonance can also be attained by the process of air compression. After all, there are some possible paths for potential study build upon the described technique:

- Based on the described method, the stiffness of the air in the cylinder itself can be exploited to achieve resonance. In this case, the influence of pressure on the natural frequency of the system is taken into account;
- In most cases of compressor systems, the prime mover might have a constant idling speed. If particular pressure demand is required to maintain resonance, spring stiffness ought to be changed correspondingly. In the forthcoming study, an adjustable spring stiffness mechanism with a control algorithm might be developed to improve the presented resonance slider-crank system capability. For compressors driven by variable speed motors, the motor speed can be directly matched to the resonant frequency, i.e., by the frequency tracking control system.

The method might further be applied and explored in functional applications such as industrial crosshead compressors. In compressors of this type, the share of mass forces is greater, and the forces occurring in the crank-slider mechanism determine the wear and durability of individual elements.

Mechanical resonance can also be used to accumulate energy in mechanical presses. Energy in such machines can be stored in a resonant block similar to flywheels. The forces acting on the crank-slider system in a mechanical press are impulse in nature, thanks to which it is possible to receive and accumulate energy sequentially with lower power demand.

Author Contributions: W.F.; Writing—Review and Editing, Conceptualization, Methodology, Resources, Validation, Supervision. W.P.; Writing—Original Draft, Writing—Review and Editing, Methodology, Formal analysis, Investigation, Software, Data Curation, Visualization. All authors have read and agreed to the published version of the manuscript.

Nomenclature

$\dot{m}_d$	mass flow rate at the outlet	θ_G	lowest possible angular displacement of the connecting rod relative to the horizontal axis of joint C
h_1	relative height of the crank CM to its lowest position due to gravity	μ_d	coefficient of dynamic friction
h_2	relative height of the connecting rod CM to its lowest position due to gravity	μ_s	coefficient of static friction
F_l	peak load at the top of the piston	τ_{RMS}	crankshaft RMS torque
I_j	moment of inertia of the component	ω_0	natural frequency or undamped angular frequency
P_{avg}	average power consumption	ω_r	resonant frequency
c_b, c_s, c_p	constants that are related to the damping coefficients of the bearing, crosshead, and piston, respectively	Δp	valve net opening pressure
c_j	constants that are related to the damping coefficients	$\mathcal{L}$	the Lagrangian
d_p	piston diameter	G	relief valve mass flow rate pressure gradient
d_r	rod diameter	M	total reciprocating mass
l_1	crank radius	P	external force
l_2	connecting rod length	R	specific gas constant
m_j	center of mass (CM) of the component	T	kinetic energy; temperature
o_v	fractional valve opening	V	potential energy; volume of chamber
p_1	pressure at the outlet side	g	gravity acceleration
p_2	pressure at the inlet side	k	spring constant
p_c	cracking pressure	k_{eq}	total (equivalent) spring constant
p_d	pressure drop	p	pressure
p_l	pressure at the top of the piston	s	current chamber length
p_{max}	maximum opening pressure	x	translational displacement of reciprocating masses
$q_j, \dot{q}_j$	generalized coordinate and velocity, respectively	$\mathcal{D}$	dissipation function
r_1	distance of crank CM to joint A	$\alpha, \dot{\alpha}, \ddot{\alpha}$	angular displacement, velocity, and acceleration, respectively, of crank on joint A
r_2	distance of connecting rod CM to joint C	$\beta, \dot{\beta}$	angular displacement, and velocity, respectively, of connecting rod on joint C
x_0	chamber length at zero displacement	ω	crankshaft angular velocity, similar to $\dot{\alpha}$

References

1. Nacions Unides., Assemblea General. *Transforming Our World the 2030 Agenda for Sustainable Development*; Nacions Unides., Assemblea General: New York, NY, USA, 2015.
2. Sheu, D.D. Overall input efficiency and total equipment efficiency. *IEEE Trans. Semicond. Manuf.* **2006**, *19*, 496–501. [CrossRef]
3. Alsyouf, I. The role of maintenance in improving companies' productivity and profitability. *Int. J. Prod. Econ.* **2007**, *105*, 70–78. [CrossRef]
4. Skorek, G. Study of losses and energy efficiency of hydrostatic drives with hydraulic cylinder. *Pol. Marit. Res.* **2018**, *25*, 114–128. [CrossRef]
5. Mori, M.; Fujishima, M.; Inamasu, Y.; Oda, Y. A study on energy efficiency improvement for machine tools. *CIRP Ann.* **2011**, *60*, 145–148. [CrossRef]
6. Xu, W.; Cao, L. Energy efficiency analysis of machine tools with periodic maintenance. *Int. J. Prod. Res.* **2014**, *52*, 5273–5285. [CrossRef]
7. Daniel, G.B.; Cavalca, K.L. Analysis of the dynamics of a slider–crank mechanism with hydrodynamic lubrication in the connecting rod–slider joint clearance. *Mech. Mach. Theory* **2011**, *46*, 1434–1452. [CrossRef]
8. Ni, L.; Huang, Y.Y.; Zhou, C.K. The dynamic simulation of Engine Slider-Crank mechanism based on ANSYS and adams. *Adv. Mater. Res.* **2013**, *842*, 347–350. [CrossRef]
9. Hroncová, D.; Binda, M.; Šarga, P.; Kičák, F. Kinematical analysis of crank slider mechanism using MSC ADAMS/View. *Procedia Eng.* **2012**, *48*, 213–222. [CrossRef]
10. Arakelian, V. Design of Torque-Compensated Mechanical Systems With Two Connected Identical Slider-Crank Mechanisms. *J. Mech. Robot.* **2021**, *14*, 024503. [CrossRef]
11. Pishvaye Naeeni, I.; Keshavarzi, A.; Fattahi, I. Parametric Study on the Geometric and Kinetic Aspects of the Slider-Crank Mechanism. *Iran. J. Sci. Technol. Trans. Mech. Eng.* **2018**, *43*, 405–417. [CrossRef]
12. Hasan, M.H.; Alsaleem, F.M.; Jaber, N.; Hafiz, M.A.A.; Younis, M.I. Simultaneous electrical and mechanical resonance drive for large signal amplification of micro resonators. *AIP Adv.* **2018**, *8*, 015312. [CrossRef]
13. Chow, L.S.; Paley, M.N. Recent advances on optic nerve magnetic resonance imaging and post-processing. *Magn. Reson. Imaging* **2021**, *79*, 76–84. [CrossRef] [PubMed]
14. Michel, D.; Xiao, F.; Alameh, K. A compact, flexible fiber-optic Surface Plasmon Resonance sensor with changeable sensor chips. *Sens. Actuators B Chem.* **2017**, *246*, 258–261. [CrossRef]
15. Li, W.; Liu, Y.; Ge, S.; Liao, D. Research of Mechanical Resonance Analysis and Suppression Control Method of the Servo Drive System. *Shock. Vib.* **2021**, *2021*, 1–15. [CrossRef]
16. Woo, T.G.; Kim, B.J.; Yoon, Y.D. Mechanical resonance suppression method based on active disturbance rejection control in two-mass servo system. *J. Power Electron.* **2022**, *22*, 1324–1333. [CrossRef]
17. Li, X.; Zhou, W.; Luo, J.; Qian, J.; Ma, W.; Jiang, P.; Fan, Y. A New Mechanical Resonance Suppression Method for Large Optical Telescope by Using Nonlinear Active Disturbance Rejection Control. *IEEE Access* **2019**, *7*, 94400–94414. [CrossRef]
18. Sinha, J.K.; Rao, A.R. Vibration diagnosis of failure of mechanical coupling between motor and pump rotors. *Int. J. Acoust. Vib.* **2005**, *10*, 89–92. [CrossRef]
19. Ghemari, Z.; Salah, S.; Bourenane, R. Resonance effect decrease and accuracy increase of piezoelectric accelerometer measurement by appropriate choice of frequency range. *Shock. Vib.* **2018**, *2018*, 1–8. [CrossRef]
20. El-Gazzar, D.M. Finite element analysis for structural modification and control resonance of a vertical pump. *Alex. Eng. J.* **2017**, *56*, 695–707. [CrossRef]
21. Franca, L.F.; Weber, H.I. Experimental and numerical study of a new resonance hammer drilling model with drift. *Chaos Solitons Fractals* **2004**, *21*, 789–801. [CrossRef]
22. Despotovic, Z.; Sinik, V.; Ribic, A. The impact of switch mode regulated vibratory resonance conveyors with electromagnetic drive on the power supply network. In Proceedings of the 2012 15th International Power Electronics and Motion Control Conference (EPE/PEMC), Novi Sad, Serbia, 4–6 September 2012. [CrossRef]
23. Aiple, M.; Smisek, J.; Schiele, A. Increasing Impact by Mechanical Resonance for Teleoperated Hammering. *IEEE Trans. Haptics* **2019**, *12*, 154–165. [CrossRef]
24. Fiebig, W.; Wróbel, J. Energy accumulation in mechanical resonance and its use in drive systems of impact machines. *Arch. Civ. Mech. Eng.* **2020**, *20*, 1–11. [CrossRef]
25. Bödrich, T. System and Component Design of Directly Driven Reciprocating Compressors with Modelica. In Proceedings of the Modelica Association, Vienna, Austria, 4–5 September 2006; pp. 421–430. Available online: https://www.semanticscholar.org/paper/System-and-Component-Design-of-Directly-Driven-with-B%C3%B6drich/9ffd7c10f162c72b88a91448c138e47cf3caec2e (accessed on 27 February 2021).
26. Arakelian, V.; Briot, S. Simultaneous inertia force/moment balancing and torque compensation of slider-crank mechanisms. *Mech. Res. Commun.* **2010**, *37*, 265–269. [CrossRef]
27. Lew, S. CAD File of AC Asynchronous Motor. Retrieved 4 May 2019. Available online: https://grabcad.com/library/ac-asynchronous-motor-1 (accessed on 27 February 2021).
28. McConville, J.B. *Introduction to Mechanical System Simulation Using Adams*; SDC Publications: Mission, KS, USA, 2015.

29. Jia, B.; Mikalsen, R.; Smallbone, A.; Roskilly, A.P. A study and comparison of frictional losses in free-piston engine and crankshaft engines. *Appl. Therm. Eng.* **2018**, *140*, 217–224. [CrossRef]
30. Trivedi, H.; Bhatt, D. Effect of lubricants on the friction of cylinder liner and piston ring materials in a reciprocating bench test. *FME Trans.* **2019**, *47*, 23–28. [CrossRef]
31. Hirani, H.; Samanta, P. Hybrid (hydrodynamic + permanent magnetic) journal bearings. *Proc. Inst. Mech. Eng. Part J. J. Eng. Tribol.* **2007**, *221*, 881–891. [CrossRef]
32. JTEKT Corporation. *Koyo: Ball & Roller Bearings*; JTEKT Corporation: Greenville, SC, USA, 2021; Available online: https://koyo.jtekt.co.jp/en/support/catalog-download/ (accessed on 27 February 2021).
33. Xu, W.; Wang, Q.; Li, X.; Liu, Y.; Zhu, J. A novel resonant frequency tracking control for linear compressor based on MRAS method. *CES Trans. Electr. Mach. Syst.* **2020**, *4*, 227–236. [CrossRef]